# Terahertz radiation-induced conductivity, Kerr and Faraday angles, and spin textures in a two-dimensional electron gas with spin-orbit coupling subjected to a high magnetic field and periodic potential

A. A. Perov, L. V. Solnyshkova, and D. V. Khomitsky*
*Department of Physics, University of Nizhny Novgorod, 23 Gagarin Avenue, 603950 Nizhny Novgorod, Russian Federation*
(Received 27 May 2010; revised manuscript received 21 September 2010; published 22 October 2010)

The terahertz radiation-induced conductivity and dielectric polarization tensors as well as the Faraday and Kerr rotation angles and the nonequilibrium spin textures are studied for two-dimensional electron gas with strong spin-orbit coupling subjected to high magnetic field and to tunable periodic potential of a two-dimensional gated superlattice. It is found that both real and imaginary parts of the frequency-dependent induced conductivity approach maximum values with sharp and detectable peaks at frequencies corresponding to the intersubband transitions between spin-split magnetic subbands. The observed properties of the conductivity tensor frequency dependence are applied for the description of the Kerr and Faraday rotation angles which can be used as another experimental tool for describing the electron gas in periodic structures with significant spin-orbit coupling. The formation of radiation-induced spin textures is predicted having both in-plane and out-of-plane components with space distribution scale comparable to the superlattice cell size which can be observed experimentally.

DOI: 10.1103/PhysRevB.82.165328 PACS number(s): 73.21.Cd, 75.70.Tj, 78.67.Pt

## I. INTRODUCTION

In recent years the spin-dependent properties of heterostructures with Rashba[1] or Dresselhaus[2] spin-orbit coupling (SOC) have attracted considerable attention in both fundamental and applied areas of condensed-matter physics studying the spin-related phenomena and known as spintronics.[3–5] The interest in SOC-related effects in semiconductor physics originates from a promising idea of the spin control without an external magnetic field variations as it was proposed, for example, by Datta and Das[6] in their scheme of a spin field-effect transistor. Besides the transport measurements and the physics of the spin or charge transfer, the properties of semiconductor heterostructures with SOC caused by an external electromagnetic radiation have also been the topic of an extensive research. The attention given to the radiation-induced properties is natural since, on the one hand, the associated experiments are the usual and reliable tool for determination of various material parameters in condensed-matter physics, and, on another hand, a proposal and observation of new externally triggered effects in heterostructures is always of interest for both fundamental problems of condensed-matter physics and for the technological applications.[3–5] These effects are very versatile in their nature and have different measurable parameters, and here we shall focus mainly on the radiation-induced conductivity tensor, on the dielectric matrix, and on the associated Faraday and Kerr rotation angles as well as on the excited nonequilibrium spin textures. The major part of the research in this field considered the metal-based or magnetic semiconductor structures where the conductivity tensor and Kerr effect have been considered,[7–20] although the magneto-optical properties of the molecular semiconductors[21] and for the systems in the quantum-Hall-effect regime have also been studied.[22] Similar effects in nonmagnetic semiconductor structures have also been explored, including the Faraday[14,23] and Kerr[24,25] effects as well as their properties in the presence of a significant SOC in two-dimensional electron gas (2DEG) (Ref. 26) and the field-induced nonequilibrium spin density.[27–29,32]

Among the various ways of constructing the heterostructure systems with novel properties of quantum states, transport, dynamical, and spin-related effects the formation of 2DEG with lateral gated superlattice provides a flexible tool also for the semiconductors with strong SOC. It is well known that an external electromagnetic field can generate novel effects including spin-current injection[30,31] and spin polarization[5,32]in systems with significant SOC. This has been also demonstrated in SOC superlattices where the properties of quantum states, dynamical and transport properties together with the radiation-induced spin textures have been investigated in one-dimensional (1D) superlattices without magnetic field,[33] and the quantum states and quantization of Hall conductance together with magneto-optical properties were studied in 2D superlattices at high magnetic field,[34,35] respectively. It was found that the gate control together with the external dc electric or electromagnetic excitation can provide new possibilities of controllable manipulations of energy spectrum, charge and spin densities, and the Hall conductivity. Thus, it is of interest to make a step further and to consider the microwave conductance and dielectric matrices together with the excited spin textures for 2DEG with SOC subjected to a high magnetic field and to the tunable periodic potential of a 2D gated superlattice. The properties of energy spectrum and spinor wave functions for such system as well as the dc Hall conductance[34] and magneto-optical absorption[35] have already been studied in detail for both Rashba and Dresselhaus contributions to SOC. The calculations of the magneto-optical conductivity and dielectric tensors and the discussion of the associated Faraday and Kerr effects together with the excited spin textures in such structures are the primary goals of the present paper. We shall focus here on the parameters of the InGaAs/GaAs 2DEG structure with dominating Rashba SOC and on the frequency range of external electromagnetic radiation which may pro-

 

vide the best characteristics of these effects for possible experimental observation and technological applications.

The paper is organized as follows: in Sec. II we briefly describe the Hamiltonian and the quantum states in our system, in Sec. III we calculate and discuss the radiation-induced conductivity and dielectric matrices which are applied in Sec. IV for the calculation of Kerr and Faraday rotation angles, in Sec. V we focus on the induced nonequilibrium spin density forming the spin textures, and the concluding remarks are given in Sec. VI.

## II. HAMILTONIAN AND QUANTUM STATES

We consider the 2DEG in the $(x,y)$ plane in a InGaAs/GaAs heterostructure with the In content of around 0.23, where the electron effective mass and $g$-factor are $m^*=0.05m_0$ and $g=-4.0$, respectively, and the SOC is dominated by the Rashba term with a significant amplitude $\alpha=2.5\times10^{-9}$ eV cm.

The corresponding one-electron Hamiltonian has the following form:[34]

$$\hat{H}=\frac{1}{2m^*}(\hat{\mathbf{p}}-e\mathbf{A}/c)^2\hat{E}+\frac{\alpha}{\hbar}[\mathbf{z}\times\hat{\sigma}]\cdot\left(\hat{\mathbf{p}}-\frac{e}{c}\mathbf{A}\right)-\frac{1}{2}g\mu_B H\hat{\sigma}_z+V(x,y)\hat{E}. \quad (1)$$

Here $\hat{p}_{x,y}$ are the momentum operator components, $m^*$ is the electron effective mass, $\hat{\sigma}_i$ are the Pauli matrices, $\alpha$ is the strength of Rashba SO coupling term, $g$ is the Landè factor, $\mu_B$ is the Bohr magneton, and $\hat{E}$ is the unit matrix. We use the Landau gauge in which the vector potential of the static magnetic field has the form $\mathbf{A}=(0,Hx,0)$, and consider a simple form of the periodic superlattice potential $V(x,y)=V_0(\cos 2\pi x/a+\cos 2\pi y/a)$ with amplitude $V_0$ and the superlattice period $a$. The structure of the Hamiltonian matrix as well as the matrix elements have been discussed in detail in our previous papers.[34,35] It was demonstrated that the SOC mixes the states of pure Landau levels and results in a doubling of the number of the magnetic subbands formed under the fixed value $p/q$ of magnetic flux quanta $\Phi/\Phi_0=p/q=|e|Ha^2/2\pi\hbar c$ ($p$ and $q$ are prime integers) per unit cell. For a given magnetic flux $p/q$ the spectrum of Hamiltonian (2) consists of magnetic subbands on the distance of the order $V_0$ near the corresponding Landau levels, each being split by the Zeeman and by the SOC terms.

As to the structure of the eigenstate of the Hamiltonian (2), one can express them as a set of two-component spinors where each component satisfies the generalized Bloch-Peierls conditions in the magnetic elementary cell which is the initial superlattice cell multiplied by the factor of $q$ in $x$ direction if the Landau gauge $\mathbf{A}=(0,Hx,0)$ is chosen. Correspondingly, the magnetic Brillouin zone is determined by inequalities $-\pi/qa\le k_x\le\pi/qa$, $-\pi/a\le k_y\le\pi/a$, and a two-component spinor wave function has the following form:[34,35]

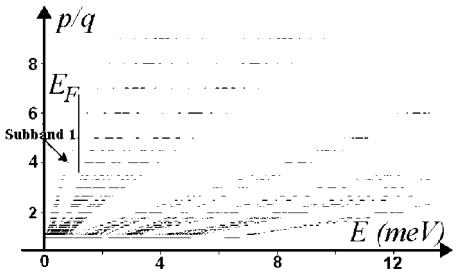


FIG. 1. Energy spectrum versus the magnetic flux $p/q$ for two lowest Zeeman and Rashba SOC-split Landau levels the 2DEG in InGaAs/AlGaAs 2D superlattice with Rashba SOC $\alpha=2.5\times10^{-9}$ eV cm. The electron effective mass $m^*=0.05\ m_0$ and the superlattice period and amplitude $a=80$ nm and $V_0=1$ meV. Below the effects for subbands at $p/q=4/1$ corresponding to the magnetic field $H\approx2.6$ T are considered with the Fermi level located in the gap above the lowest subband 1 marked by arrow.

$$\Psi_{\mathbf{k}}(\mathbf{r})=\frac{1}{La\sqrt{q}}\sum_{l=-L/2}^{L/2}\sum_{n=1}^{p}e^{ik_x(lqa+nqa/p)}e^{2\pi iy(lp+n)/a}\times e^{ik_y y}\left\{A_n(\mathbf{k})\Phi_0\left(\frac{x-x_0-lqa-nqa/p}{l_H}\right)\begin{pmatrix}0\\1\end{pmatrix}+B_n(\mathbf{k})\frac{1}{\sqrt{1+D_1^2}}\begin{bmatrix}\Phi_0\left(\frac{x-x_0-lqa-nqa/p}{l_H}\right)\\-D_1\Phi_1\left(\frac{x-x_0-lqa-nqa/p}{l_H}\right)\end{bmatrix}\right\}. \quad (2)$$

Here, $D_1=\alpha\sqrt{2}/[l_H(E_0^+ + \sqrt{E_0^{+2}+2\alpha^2/l_H^2})]$, $\Phi_{0,1}[\xi]$ are the simple harmonic oscillator functions, $l_H=c\hbar/|e|H$ is the magnetic length, $E_0^+=\frac{\hbar\omega_c}{2}+\frac{1}{2}g\mu_B H$ and $\omega_c=|e|H/m^*c$ is the cyclotron frequency, $\xi_{\ell n}=(x-x_0-\ell qa-nqa/p)/l_H$, $x_0=c\hbar k_y/|e|H$, and $L$ is the sample size in the $y$ direction which accounts for the wave function norm. The expansion coefficients $A_n(\mathbf{k})$ and $B_n(\mathbf{k})$ in Eq. (5) are defined together with the energy eigenvalues during the standard diagonalization procedure for the Schröedinger equation.

An example of the energy spectrum considered for the following calculations is shown in Fig. 1 for the magnetic flux region with $p/q=4/1$ corresponding to $H\approx2.6$ T and for the superlattice potential amplitude $V_0=1$ meV. Here the periodic potential amplitude $V_0$ and the SOC energy have the same order, so the inequality $\Delta E_{SO}\simeq V_0\le\hbar\omega_c$ takes place, and one can use a two-level approximation, where the higher Landau levels do not provide a significant contribution to the quantum states and the associated effects for two lowest Landau levels. Below we set $p/q=4/1$ corresponding to the magnetic field $H\approx2.6$ T in a superlattice with period $a=80$ nm, and the Fermi level is located in the gap above the lowest subband 1 marked by arrow in Fig. 1. One can see that the photon energy for the intersubband transitions here is of the order of 1 meV corresponding to the frequency $\nu\sim10^{12}$ s$^{-1}$ which is the terahertz range being of high interest

for the current research in magneto-optical properties of semiconductor heterostructures. In a real semiconductor structure with SOC superlattice such position of the Fermi level corresponds to the concentrations of about $10^{10},\ldots,10^{11}$ cm$^{-2}$. Of course, the manifestation of such tiny and fragile miniband structure as on Fig. 1 in measurable experimental phenomena requires the preparation of high-purity samples and low temperatures inside experimental setups which, as it is known, is still a conventional condition for monitoring the SOC-related effects in GaAs-based semiconductors where the SOC is relatively weak.

## III. MICROWAVE CONDUCTIVITY AND DIELECTRIC TENSORS

In this section we shall consider the microwave conductivity and dielectric tensors describing the effects of perturbation caused by the external monochromatic and linearly polarized electromagnetic field with vector potential $\mathbf{A}_\omega=(A_\omega,0,0)$, where $A_\omega=A_0\exp[i(\mathbf{k}\cdot\mathbf{r}-\omega t)]$. Under the dipole approximation the amplitude of the photon wave vector is negligible compared to the electron quasimomentum which leads to the following form of the perturbation Hamiltonian $\hat{H}_{\rm int}$ in the presence of the Rashba SOC:

$$\hat{H}_{\rm int}=-\frac{i|e|\hbar}{m^*c}A_0e^{-i\omega t}\frac{\partial}{\partial x}-\frac{|e|}{c}\frac{\alpha}{\hbar}A_0e^{-i\omega t}\hat{\sigma}_y. \tag{3}$$

The main distinguishable property of Eq. (6) compared to the system without SOC is the presence of second term which is spin dependent and linear in the Rashba SOC strength. The SOC also introduces the spin-dependent term into the velocity operator $\hat{\mathbf{v}}=(i/\hbar)[\hat{H},\mathbf{r}]$ which components $\hat{v}_{x,y}$ in the basis of the $\hat{\sigma}_z$ eigenstates have the following matrix form:

$$\hat{v}_x=\begin{pmatrix}-i\hbar\nabla_x/m^* & i\alpha/\hbar\\ -i\alpha/\hbar & -i\hbar\nabla_x/m^*\end{pmatrix}, \tag{4}$$

$$\hat{v}_y=\begin{pmatrix}-i\hbar\nabla_y/m^*-\omega_c x & \alpha/\hbar\\ \alpha/\hbar & -i\hbar\nabla_y/m^*-\omega_c x\end{pmatrix}. \tag{5}$$

With the known eigenfunctions in Eq. (5) the matrix elements in Eqs. (7) and (8) can be expressed directly via the wave function coefficients $A(\mathbf{k})$ and $B(\mathbf{k})$ as

$$v^x_{\mathbf{k}\nu\mu}=\sum_{n,m=1}^{p}\frac{i}{\sqrt{1+D_1^2}}[A_n^{\nu*}(\mathbf{k})B_m^{\mu}(\mathbf{k})-B_n^{\nu*}(\mathbf{k})A_m^{\mu}(\mathbf{k})]\left(\frac{D_1\hbar}{m^*}\sqrt{\frac{\pi p}{q}}-\frac{\alpha}{\hbar}\right), \tag{6}$$

$$v^y_{\mathbf{k}\nu\mu}=\sum_{n,m=1}^{p}\frac{1}{\sqrt{1+D_1^2}}\left\{\frac{\alpha}{\hbar}[A_n^{\nu*}(\mathbf{k})B_m^{\mu}(\mathbf{k})+B_n^{\nu*}(\mathbf{k})A_m^{\mu}(\mathbf{k})]+\frac{i\hbar D_1}{m^*l_H\sqrt{2}}[A_n^{\nu*}(\mathbf{k})B_m^{\mu}(\mathbf{k})-B_n^{\nu*}(\mathbf{k})A_m^{\mu}(\mathbf{k})]\right\}-\frac{k_y\hbar}{m^*}[A_n^{\nu*}(\mathbf{k})A_m^{\mu}(\mathbf{k})+B_n^{\nu*}(\mathbf{k})B_m^{\mu}(\mathbf{k})], \tag{7}$$

which allows to calculate explicitly the components of the conductivity tensor $\sigma_{ij}(\omega)$ for the frequency range $\nu\sim0.1,\ldots,1.0$ THz corresponding to the transitions between the magnetic subband 1 below the Fermi level and the subbands above the Fermi level shown in Fig. 1. The expression for $\sigma_{ij}(\omega)$ can be derived from the Kubo formula[36] and is applied for our calculations in the following form:[7,11,18,36,37]

$$\sigma_{ij}(\omega)=\frac{e^2}{8\pi\hbar\omega}\sum_{\mathbf{k},\mu,\nu}v^i_{\mathbf{k}\mu\nu}v^j_{\mathbf{k}\nu\mu}f_{\mathbf{k}\mu}(1-f_{\mathbf{k}\nu})\delta(E_{\mathbf{k}\nu}-E_{\mathbf{k}\mu}-\hbar\omega), \tag{8}$$

where (per unit volume) at zero temperature the sum is taken over all states with energy $E_{\mathbf{k}\mu}$ below and above the Fermi level, respectively, by applying the Fermi distribution function $f_{\mathbf{k}\nu}$. The expression (8) is written for the absence of scattering, i.e., for the infinite lifetime of the extended Bloch states.[18] It can be verified that this approximation remains qualitatively valid for finite lifetime also as long as the subband broadening for the spectrum shown in Fig. 1 does not exceed the intersubband spacing which can be achieved in clean heterostructures at low temperatures, where the manifestation of the magnetic subband fine structure is visible.[34] It should be mentioned also that the longitudinal part $\sigma_{xx}$ of Eq. (8) is real while the off-diagonal part $\sigma_{xy}$ has both real and imaginary parts which is a usual property of the radiation-induced conductivity.

The knowledge of the conductivity tensor in Eq. (8) allows us to calculate directly the components of the frequency-dependent dielectric tensor $\varepsilon_{ij}(\omega)$ via a conventional relation

$$\varepsilon_{ij}(\omega)=\delta_{ij}+\frac{4\pi i}{\omega}\sigma_{ij}(\omega). \tag{9}$$

In Fig. 2 we show the frequency dependence of real and imaginary parts of (a) $\sigma_{xx}$, $\sigma_{xy}$ and (b) $\varepsilon_{xx}$, $\varepsilon_{xy}$ which are the only non-vanishing components for the incident radiation linearly polarized along $x$ axis and propagating perpendicular to the 2DEG. The bulk dimension of $\sigma_{ij}$ in s$^{-1}$ corresponds to our understanding of the system as having a finite layer thickness parameter which enters below in the corresponding expressions for the Faraday and Kerr rotation angles which typically include such a characteristic of the system as the traveling distance or thickness. By analyzing Fig. 2 one can see that the components of both the conductivity and the dielectric tensors reach their local maximum values at frequencies corresponding to the distance between centers of the magnetic subbands shown in Fig. 1. One can see that the induced off-diagonal component $\varepsilon_{xy}(\omega)$ of the dielectric tensor at certain frequencies can be quite significant and reach the magnitude of the order of 0.5 which is a sizable off-diagonal contribution to the static dielectric constant which is about 12.5.[38] The detailed structure of the conductivity plots in Fig. 2(a) near $\nu=0.28$ THz, where some of the conductivity components change their sign is marked by rectangle and will be discussed below. The practical value of the results shown in Fig. 2 is well known: since the measurements of the radiation-induced conductivity are among the most popular experimental tools for determining the param-

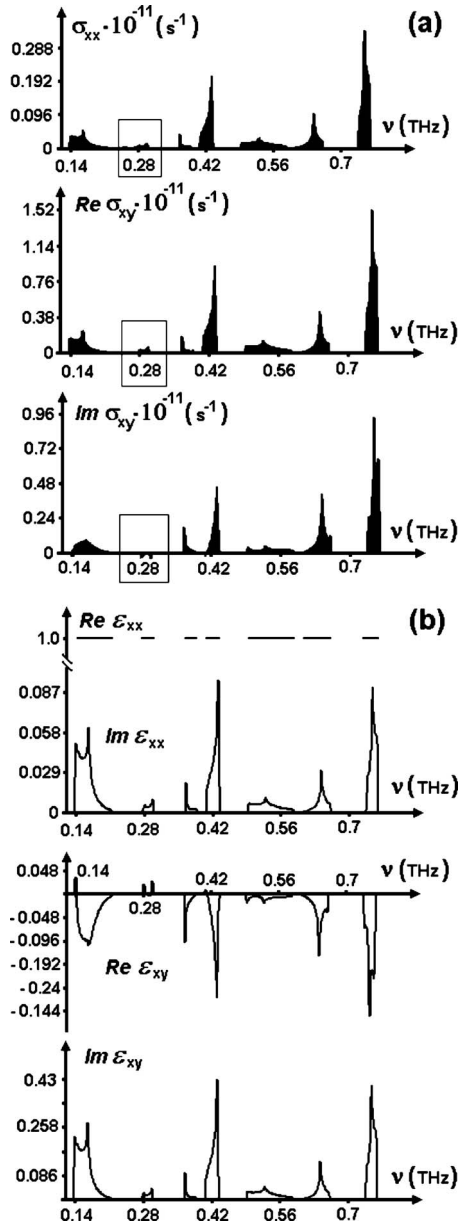


FIG. 2. Frequency dependence of (a) $\sigma_{xx}$, real and imaginary parts of $\sigma_{xy}$ and (b) the same for $\varepsilon_{xx}$, $\varepsilon_{xy}$ for the incident radiation linearly polarized along $x$ axis and propagating perpendicular to the 2DEG. The components of both the conductivity and the dielectric tensors have their maxima at frequencies corresponding to the distance between centers of the magnetic subbands shown in Fig. 1. The detailed structure near $\nu=0.28$ THz marked by rectangle is discussed below.

eters of heterostructures, our calculations provide a useful prediction of experimentally measurable quantities suitable for description of actually used structures with strong SOC.

The detailed structure of the photon energy dependence of the conductivity and dielectric tensor components shown in Fig. 2 can be clarified to some extent if we consider it together with the energy dispersion relations in those subband pairs which are relevant for the given part of the photon frequency range. In Fig. 3 we show the $k_x$-dependence of the energy difference $E_{13}(k_x,k_y)=E_1(k_x,k_y)-E_3(k_x,k_y)$ between

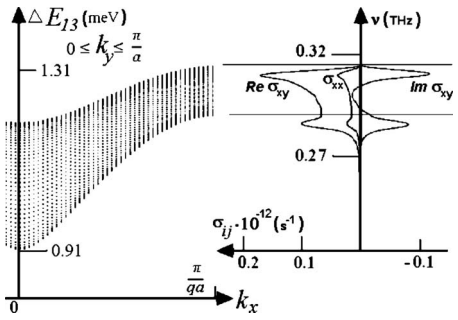


FIG. 3. (Left) The $k_x$ dependence of the energy difference $E_{13}(k_x,k_y)=E_3(k_x,k_y)-E_1(k_x,k_y)$ between the subbands 1 and 3 for to the frequency range on the inset in Fig. 2 and (right) the corresponding photon energy dependence of the conductivity tensor components. The points where the Im $\sigma_{xy}$ component changes its sign correspond to the areas in $E_{13}$ plot where the curvature of the $E_{13}(k_x,k_y)$ function changes its sign.

the subbands 1 and 3 corresponding to the frequency range on the inset in Fig. 2. The whole energy range is covered by running the $k_y$ component over half on the Brillouin zone range $0\leq k_y\leq \pi/a$, and the $k_x$ component in Fig. 3 varies between 0 and $\pi/qa$ (here $q=1$) since the subband energy spectrum $E_m(k_x,k_y)$ in the square lattice with Rashba SOC is invariant under the transformations $k_{x,y}\rightarrow -k_{x,y}$.[34] By comparing the energy dispersion on the left side of Fig. 3 with the conductivity frequency dependence on the right side plotted on the same energy scale one can connect some specific points of the conductivity plots with the properties of the energy difference dispersion relation. In particular, the points where the imaginary part of $\sigma_{xy}$ component responsible for the direction of Kerr angle changes its sign clearly corresponds to the areas in the plot for the energy difference function $E_{13}=E_3-E_1$ for the subbands 1 and 3, respectively, where the second-order derivatives, i.e., the curvature of the $E_{13}(k_x,k_y)$ function changes its sign. Such connections between the conductivity and the dispersion relations are not uncommon[33,34] since the former is determined in Eq. (8) via the matrix elements of the velocity operators which, in turn, depend on the shape of the dispersion relation $E_m(k_x,k_y)$ in the particular $m$th miniband. The example shown in Fig. 3 once again demonstrates the importance of the conductivity tensor calculations since its experimental measurement is possible and may provide us with certain information about the topological structure of the energy subbands of such nontrivial system as the 2D superlattice with Rashba SOC in the magnetic field considered here.

## IV. FARADAY AND KERR ROTATION ANGLES

The knowledge of the radiation-induced conductivity tensor $\sigma_{ij}(\omega)$ can be applied for determination of (depending on the setup) the Kerr or Faraday rotation angles which are often used for experimental characterization of various heterostructures.[7–13,15–19] Since the most straightforward manifestation of the Faraday or Kerr rotation is the rotation of the polarization plane on a specific angle, we consider in our manuscript the linearly polarized incident radiation in-

coming perpendicular to the 2DEG plane $(xy)$ with the electric field vector parallel to the $x$ axis, $\mathbf{E}=(E_x,0,0)$. The interaction of external field with the media may generate the $y$ component of the electric field which corresponds to the rotation angle $\theta$ described simply as[22] $\tan(\theta)=E_y/E_x$. It is clear that although this rotation angle arises due to the application of the external field, its magnitude is not directly related to the strength of the field components $E_{x,y}$ due to the expression with a fraction where the common field amplitude is cancelled and thus can be measurable even for moderated excitation amplitudes. It is known that the rotation angle can be defined as the rotation per unit distance traveled by the incident wave without taking into account a specific thickness of the structure.[23] In this paper we apply the term "2DEG;" however, one should keep in mind that it is essentially contained in a triangular InGaAs/GaAs quantum well with finite thickness $d$ which value affects the actual rotation angle as the travel distance. In the following calculations we use a typical value $d=100$ nm and we apply an expression for the Faraday rotation angle derived for a thin film with thickness $d$ (here $d \ll \lambda$, where $\lambda$ is the incoming wavelength) deposited on a GaAs substrate with the index of refraction $n_s \approx 3.5$ (Ref. 38) which has the following form:[17,22,23]

$$\theta_F \approx \frac{\mathrm{Re}(\sigma_{xy})}{\sigma_{xx}}\left[1+\frac{1}{Z_+\sigma_{xx}}\right]^{-1}, \tag{10}$$

where $Z_\pm = d/[c(n_s \pm 1)]$. The Faraday effect involves the transmission of the incident radiation and one has the real part of the off-diagonal conductivity present in Eq. (10). It is clear that in the limit of a very thin 2DEG layer $d \to 0$ or in frequency intervals where the longitudinal conductivity $\sigma_{xx}$ drops, the Faraday angle is determined solely by the off-diagonal part of the conductivity tensor

$$\theta_F(\sigma_{xx} \to 0) \approx \mathrm{Re}(\sigma_{xy})\frac{d}{c}\frac{1}{(n_s+1)} \tag{11}$$

in accordance with what has been shown earlier.[22,23] Then, under the same approximations one can apply also the relation for Kerr angle $\theta_K$ which reads as[17]

$$\theta_K \approx \frac{\mathrm{Im}(\sigma_{xy})}{\sigma_{xx}^2}\left(-\frac{2c}{d}\right)\left[\left(1+\frac{1}{Z_+\sigma_{xx}}\right)\left(1+\frac{1}{Z_-\sigma_{xx}}\right)\right]^{-1} \tag{12}$$

and is determined by the reflection, i.e., imaginary part of the off-diagonal component of the conductivity tensor.

It is clear that here both Faraday and Kerr angles are determined by the conductivity tensor components only, and thus the frequency dependence of $\sigma_{ij}(\omega)$ discussed above and shown in Fig. 2 can be directly applied for the calculation of the frequency dependencies of the Faraday and Kerr angles which are shown in Fig. 4. A detailed comparison of Figs. 2 and 4 leads to the conclusion that the peaks of the Faraday or Kerr rotation angle correspond mainly to the intervals where at the same frequency the longitudinal conductivity $\sigma_{xx}(\omega)$ is small and the off-diagonal part $\sigma_{xy}(\omega)$ is finite, i.e., for the samples in the insulator regime where only the transverse current is induced by the external radiation. The opposite sign of the Kerr angle compared to the Faraday angle which

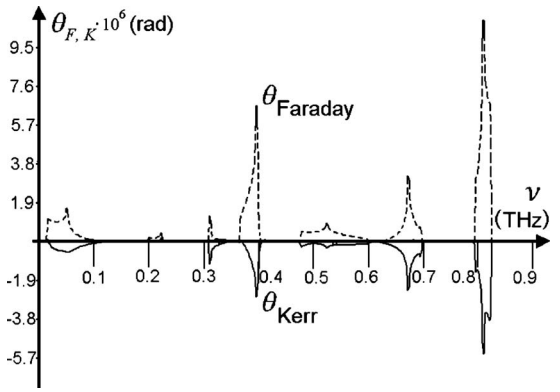


FIG. 4. Frequency dependence of the Faraday (dashed curve) and Kerr (solid curve) rotation angles for the 2DEG with Rashba SOC described by the conductivity tensor with components shown in Fig. 2. The peaks of both Faraday and Kerr rotation angle correspond to the intervals, where at the same frequency the longitudinal conductivity $\sigma_{xx}(\omega)$ is small and the off-diagonal part $\sigma_{xy}(\omega)$ is finite, i.e., for the samples in the insulator regime where only the transverse current is induced by the external radiation.

can be observed on the dominating part of the frequency range in Fig. 4 can be explained by drawing the attention to the opposite signs in the expressions (10) and (12) reflecting the additional phase rotation during the reflection for the Kerr effect compared to the absorption for the Faraday effect, and the observation that both Re $\sigma_{xy}$ and Im $\sigma_{xy}$ have mainly constant signs in the frequency regions when they are both significantly nonzero with relatively small exceptions such as the region in Fig. 3 discussed in detail above. It should be noted that the magnitude of both Faraday and Kerr angles shown Fig. 4 is rather small compared, for example with the ones for the interband transitions in ferromagnets or metal-doped semiconductors[17,18,20] while being comparable to the Faraday angle for strained GaAs or InGaAs nonmagnetic semiconductor structures,[14] to the Kerr angle in some layered metal structures[19] or organic molecular semiconductors.[21] Nevertheless, it should be stressed that the frequency dependence of Faraday or Kerr rotation angles provide a quantitative experimental tool for investigation of such fragile and sophisticated spectrum as the miniband structure of a superlattice with SOC in high magnetic field.

## V. INDUCED SPIN TEXTURES

In systems with SOC the response to the external electromagnetic radiation can be seen not only in charge but also in spin degrees of freedom. The arising nonequilibrium distributions of local spin density hereafter called the spin textures[33] are promising for further applications in spintronics and we believe that they can be probed, as any other induced magnetic polarization, by microscopic magnetization detectors[3–5] as the areas of local magnetization with spatially varying direction, by the Faraday rotation measurements[14] or Kerr microscopy.[16] Staying in the framework of the linear response theory[36] one can obtain the excited spin density in the same fashion as the charge conductivity in Eq. (8), namely,

$$S_i^j(x,y,\omega) = \frac{eE_0}{8\pi m\hbar\omega}\sum_{\mathbf{k},\mu,\nu} s^i_{\mathbf{k}\mu\nu}(x,y)v^j_{\mathbf{k}\nu\mu}f_{\mathbf{k}\mu}(1-f_{\mathbf{k}\nu}) \times \delta(E_{\mathbf{k}\nu}-E_{\mathbf{k}\mu}-\hbar\omega), \quad (13)$$

where $E_0$ is the electric field amplitude in the incident wave and the function $s^i_{\mu\nu}(x,y)$ does not include the integration over space, and thus cannot be referred as a matrix element of the spin operator but instead can be described as the position-dependent interband spin density function reading as

$$s^i_{\mathbf{k}\mu\nu}(x,y) = \psi^\dagger_{\mathbf{k}\mu}(x,y)\hat{\sigma}_i\psi_{\mathbf{k}\nu}(x,y). \quad (14)$$

The quantity $S_i^j(x,y,\omega)$ has the meaning of the local spin density created in the given point $(x,y)$ of the superlattice by the external electromagnetic radiation with frequency $\omega$ with polarization $j$ which is fixed in our problem as $j=x$, and therefore this index is omitted below. The results for induced spin texture components corresponding to two peaks of the conductivity (Fig. 2) or rotation angle (Fig. 4) frequency dependencies for $\nu=0.43$ THz and $\nu=0.64$ THz are shown below in Figs. 5 and 6, respectively, in one superlattice cell $-a/2\le x(y)\le a/2$ normalized on the superlattice unit-cell area $a^2$, i.e., the magnetic moment being actually measured by the probe with area $dS$ can be obtained after multiplying the spin density by a factor $dS/a^2$. The spin textures are shown in units for the degree of carrier polarization (i.e., in units of Bohr magneton per carrier) for the incident power of 1.0 mW/cm$^2$ which is accessible in modern experiments with nanostructures. It can be seen that all components of the induced spin density are excited on a comparable scale shown in figures (a)–(c), correspondingly which makes these predicted space distributions promising for the experimental observations.

The explanation of the rich spin texture structure can be drawn if we take into account the presence of static magnetic field along $z$ direction together with the Rashba SOC in the $(xy)$ plane which, in combinations with the linearly polarized radiation along $x$ axis may indeed create the excited spin textures with all spin components being nonzero. As to the dominating space scale of the spin texture shape which can be observed in Figs. 5 and 6, one can see that it is comparable with the superlattice size which is the lateral size of the figure being also the scale of the corresponding wave-functions shape.[34] The integration of the spin-density components in Eq. (13) over the superlattice cell indicates that all mean values for spin texture components in Figs. 5 and 6 are very close to zero. This result means that the external radiation which is treated as a perturbation provides no significant gross change in the magnetization over the whole sample but it indeed can alter the local magnetization in different parts of the structure.

The transitions corresponding to the higher frequency $\nu=0.64$ THz with spin textures in Fig. 6 occur between the lowest occupied subband 1 in Fig. 1 and higher subbands compared to the transitions with textures in Fig. 5, i.e., they are located to the right along the energy axis at the line $p/q=4/1$ in Fig. 1. The calculation of induced spin textures at different excitation frequencies is also important for possible further applications of the observed effects at variable parameters. The results for excitation frequency $\nu=0.64$ THz are shown in Fig. 6 where again (a) $S_x$, (b) $S_y$, and (c) $S_z$ spin-density components, respectively, are shown on separate plots in one square superlattice cell.

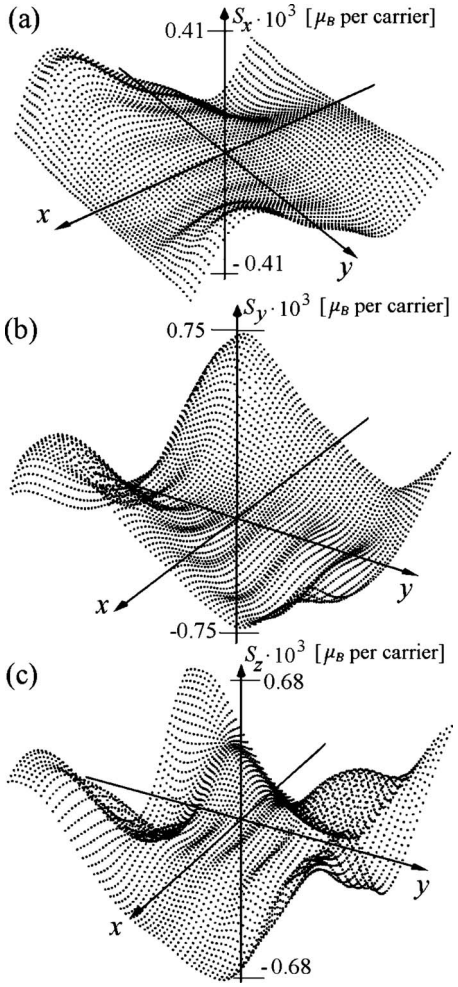


FIG. 5. Radiation-induced spin textures shown in units for the degree of carrier polarization for the incident power of 1.0 mW/cm$^2$: (a) $S_x(x,y)$, (b) $S_y(x,y)$, and (c) $S_z(x,y)$ plotted in one superlattice cell $-a/2\le x(y)\le a/2$ and normalized on the superlattice unit cell area. The presence of static magnetic field along $z$ direction together with the Rashba SOC in the $(xy)$ plane creates the excited spin textures with all spin components being of a comparable order. The dominating space scale of the spin texture shape is comparable with the superlattice size which is the lateral size of the figure.

If one compares the induced spin textures in Figs. 5 and 6 for different excitation frequencies, both common and distinct features can be found. The common features are the comparable space period and global shape of the excited textures for all spin components on both figures. This commonalty is stipulated by the common structure of initial and final quantum states for both examples including the space distribution of charge and spin density. Besides, for any excitation frequency the resulting excited spin textures is formed, in principal, by all allowed transitions between many states below and above the Fermi level, and thus one may expect

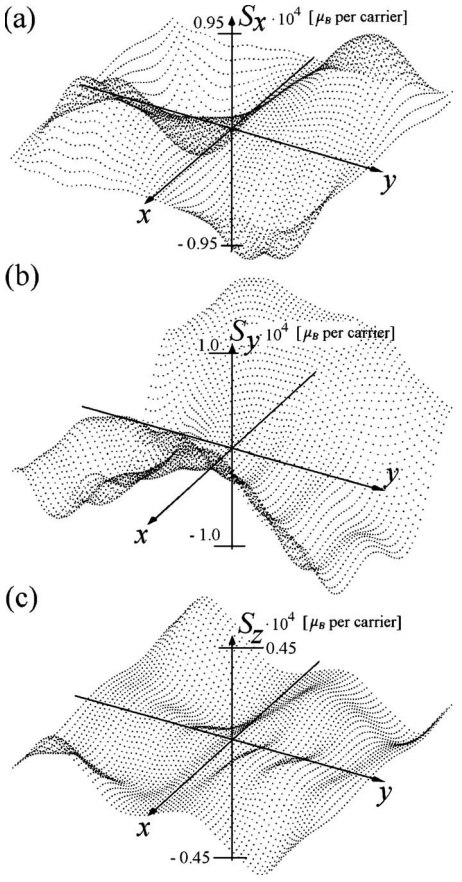


FIG. 6. The same as in Fig. 5 but for the spin textures excited by the incident radiation with the higher frequency $\nu$=0.64 THz and all other parameters remaining as in Fig. 5.

certain degree of commonalty between them.

As to the difference between the spin textures at different excitation frequencies in Figs. 5 and 6, one can observe the following. First, for the lower frequency $\nu$=0.43 THz in Fig. 5 all three excited spin components have a higher magnitude. The explanation can be obtained by taking into account the higher position in energy of the final quantum states for the induced textures in Fig. 6 which are characterized by more complicated and faster oscillating wave functions,[34,35] which, in turn, reduce the magnitude of the corresponding matrix elements and create the spin density with lower magnitude in Fig. 6 compared to Fig. 5. The same physical mechanism is responsible for the, in general, more curved shape of the spin textures in Fig. 6 compared to the ones in Fig. 5, i.e., the transitions to the quantum states with higher energy leads to the richer space shape of the excited spin textures.

It should be mentioned again that in Eq. (13) the resulting excited spin textures are formed by all allowed transitions and by many states below, and above the Fermi level and thus have an integral and pretty universal nature. First of all, this circumstance makes them robust to some extent against the possible corrections to our model, i.e., the finite sample size, the finite temperatures, the scattering on defects and phonons, and the presence of other small terms absent in our Hamiltonian. Then, these spin textures can be viewed as measurable quantities which can be obtained by a probe at a given point $(x,y)$ and thus can be considered as a promising degree of freedom for further applications such as information processing and storage in spintronics. It is interesting to note that the features of the excited spin density discussed here were also observed in qualitatively the same manifestation and with the same space shape in a different system with 2DEG and SOC subjected to periodic potential of 1D superlattice without the static magnetic field but either under scattering or under radiative (with various polarizations) or dc electric current excitation,[33] which allows to consider them as an intrinsic characteristic of low-dimensional systems with strong SOC and nonuniform periodic potential.

## VI. CONCLUSIONS

We have studied the terahertz radiation-induced conductivity and dielectric polarization tensors, the Kerr and Faraday rotation angles, and the excited spin textures for two-dimensional electron gas with strong spin-orbit coupling subjected to high magnetic field and to tunable periodic potential of a two-dimensional gated superlattice. It was found that both real and imaginary parts of the frequency-dependent conductivity approach maximum values with sharp and detectable peaks at frequencies corresponding to the intersubband transitions between spin-split magnetic subbands. The observed properties of the conductivity tensor frequency dependence were applied for the description of the Kerr and Faraday rotation angles which can be used as another experimental tool for describing the electron gas in periodic structures with significant spin-orbit coupling. The formation of radiation-induced spin textures is predicted having both in-plane and out-of-plane components with space distribution scale comparable to the superlattice cell size which can be promising in further experimental and technological applications.

## ACKNOWLEDGMENTS

The authors are grateful to V. Ya. Demikhovskii and A. M. Satanin for helpful discussions. The work was supported by the RNP Program of Ministry of Education and Science RF (Grants No. 2.1.1.2686, No. 2.1.1.3778, No. 2.2.2.2.4297, and No. 2.1.1.2833), by the RFBR (Grants No. 09-02-01241a and No. 09-01-00268a), by the USCRDF (Grant No. BP4M01), and by the President of RF Grant for Young Candidates of Science under Grant No. MK-1652.2009.2.

*Corresponding author; khomitsky@phys.unn.ru


[1] E. I. Rashba, Fiz. Tverd. Tela (Leningrad) **2**, 1224 (1960) [Sov. Phys. Solid State **2**, 1109 (1960)]; Y. A. Bychkov and E. I. Rashba, J. Phys. C **17**, 6039 (1984).

[2] G. Dresselhaus, Phys. Rev. **100**, 580 (1955).

[3] *Semiconductor Spintronics and Quantum Computation*, Nanoscience and Technology, edited by D. D. Awschalom, D. Loss, and N. Samarth (Springer, Berlin, 2002).

[4] I. Žutić, J. Fabian, and S. Das Sarma, Rev. Mod. Phys. **76**, 323 (2004).

[5] M. W. Wu, J. H. Jiang, and M. Q. Weng, Phys. Rep. **493**, 61 (2010).

[6] S. Datta and B. Das, Appl. Phys. Lett. **56**, 665 (1990).

[7] P. M. Oppeneer, T. Maurer, J. Sticht, and J. Kübler, Phys. Rev. B **45**, 10924 (1992).

[8] K. W. Wierman, J. N. Hilfiker, R. F. Sabiryanov, S. S. Jaswal, R. D. Kirby, and J. A. Woollam, Phys. Rev. B **55**, 3093 (1997).

[9] S. A. Crooker, D. D. Awschalom, J. J. Baumberg, F. Flack, and N. Samarth, Phys. Rev. B **56**, 7574 (1997).

[10] N. Richard, A. Dereux, T. David, E. Bourillot, J. P. Goudonnet, F. Scheurer, E. Beaurepaire, and G. Garreau, Phys. Rev. B **59**, 5936 (1999).

[11] V. N. Antonov, V. P. Antropov, B. N. Harmon, A. N. Yaresko, and A. Ya. Perlov, Phys. Rev. B **59**, 14552 (1999).

[12] K. Sato, A. Kodama, M. Miyamoto, A. V. Petukhov, K. Takanashi, S. Mitani, H. Fujimori, A. Kirilyuk, and T. Rasing, Phys. Rev. B **64**, 184427 (2001).

[13] J. Hamrle, J. Ferré, M. Nývlt, and Š. Višňovský, Phys. Rev. B **66**, 224423 (2002); J. Hamrle, J. Ferré, J. P. Jamet, V. Repain, G. Baudot, and S. Rousset, *ibid.* **67**, 155411 (2003).

[14] Y. K. Kato, R. C. Myers, A. C. Gossard, and D. D. Awschalom, Phys. Rev. Lett. **93**, 176601 (2004).

[15] I. Reichl, R. Hammerling, A. Vernes, P. Weinberger, C. Sommers, and L. Szunyogh, Phys. Rev. B **70**, 214417 (2004).

[16] A. Neudert, J. McCord, D. Chumakov, R. Schäfer, and L. Schultz, Phys. Rev. B **71**, 134405 (2005).

[17] M.-H. Kim, G. Acbas, M.-H. Yang, I. Ohkubo, H. Christen, D. Mandrus, M. A. Scarpulla, O. D. Dubon, Z. Schlesinger, P. Khalifah, and J. Cerne, Phys. Rev. B **75**, 214416 (2007).

[18] A. Stroppa, S. Picozzi, A. Continenza, M. Y. Kim, and A. J. Freeman, Phys. Rev. B **77**, 035208 (2008).

[19] C. Etz, A. Vernes, L. Szunyogh, and P. Weinberger, Phys. Rev. B **77**, 064420 (2008).

[20] A. Winter, H. Pascher, M. Hofmayer, H. Krenn, T. Wojtowicz, X. Liu, and J. K. Furdyna, Rev. Adv. Mater. Sci. **20**, 92 (2009).

[21] M. Fronk, B. Bräuer, J. Kortus, O. G. Schmidt, D. R. T. Zahn, and G. Salvan, Phys. Rev. B **79**, 235305 (2009).

[22] V. A. Volkov and S. A. Mikhailov, Pis'ma Zh. Eksp. Teor. Fiz. **41**, 389 (1985) [JETP Lett. **41**, 476 (1985)].

[23] L. I. Magarill and V. N. Sozinov, Pis'ma Zh. Eksp. Teor. Fiz. **52**, 1230 (1990) [J.ETP Lett. **52**, 649 (1990)].

[24] F. Teppe, M. Vladimirova, D. Scalbert, M. Nawrocki, and J. Cibert, Solid State Commun. **128**, 403 (2003).

[25] P. Olbrich, J. Allerdings, V. V. Bel'kov, S. A. Tarasenko, D. Schuh, W. Wegscheider, T. Korn, C. Schüller, D. Weiss, and S. D. Ganichev, Phys. Rev. B **79**, 245329 (2009).

[26] F. Zhang, H. Z. Zheng, Y. Li, J. Liu, and G. R. Li, EPL **83**, 47006 (2008).

[27] R. D. R. Bhat, F. Nastos, A. Najmaie, and J. E. Sipe, Phys. Rev. Lett. **94**, 096603 (2005).

[28] S. A. Tarasenko, Phys. Rev. B **72**, 113302 (2005); **73**, 115317 (2006).

[29] M. Pletyukhov and A. Shnirman, Phys. Rev. B **79**, 033303 (2009).

[30] E. Ya. Sherman, A. Najmaie, and J. E. Sipe, Appl. Phys. Lett. **86**, 122103 (2005).

[31] A. Najmaie, E. Ya. Sherman, and J. E. Sipe, Phys. Rev. Lett. **95**, 056601 (2005).

[32] J. H. Jiang, M. W. Wu, and Y. Zhou, Phys. Rev. B **78**, 125309 (2008).

[33] V. Ya. Demikhovskii and D. V. Khomitsky, Pis'ma Zh. Eksp. Teor. Fiz. **83**, 399 (2006) [JETP Lett. **83**, 340 (2006)]; D. V. Khomitsky, Phys. Rev. B **76**, 033404 (2007); **77**, 113313 (2008); **79**, 205401 (2009).

[34] V. Ya. Demikhovskii and A. A. Perov, Europhys. Lett. **76**, 477 (2006); Phys. Rev. B **75**, 205307 (2007).

[35] A. A. Perov and L. V. Solnyshkova, Pis'ma Zh. Eksp. Teor. Fiz. **88**, 717 (2008) [JETP Lett. **88**, 625 (2008)]; Fiz. Tekh. Poluprovodn. **43**, 214 (2009) [Semiconductors **43**, 202 (2009)].

[36] R. Kubo, J. Phys. Soc. Jpn. **12**, 570 (1957).

[37] C. S. Wang and J. Callaway, Phys. Rev. B **9**, 4897 (1974).

[38] Y. A. Goldberg and N. M. Schmidt, *Handbook Series on Semiconductor Parameters*, edited by M. Levinshtein, S. Rumyantsev, and M. Shur (World Scientific, London, 1999), Vol. 2, pp. 62–88.